



This is the accepted manuscript made available via CHORUS. The article has been published as:

Shapiro response of superconducting diode effect derived from Andreev molecules

Sadashige Matsuo, Russell S. Deacon, Shohei Kobayashi, Yosuke Sato, Tomohiro Yokoyama, Tyler Lindemann, Sergei Gronin, Geoffrey C. Gardner, Koji Ishibashi, Michael J. Manfra, and Seigo Tarucha

Phys. Rev. B **111**, 094512 — Published 12 March 2025

DOI: [10.1103/PhysRevB.111.094512](https://doi.org/10.1103/PhysRevB.111.094512)

Shapiro response of superconducting diode effect derived from Andreev molecules

Sadashige Matsuo^{1,2}, Russell S. Deacon^{1,3}, Shohei Kobayashi^{1,4}, Yosuke Sato¹, Tomohiro Yokoyama⁵, Tyler Lindemann⁶, Sergei Gronin⁶, Geoffrey C. Gardner⁶, Koji Ishibashi^{1,3}, Michael J. Manfra^{6,7,8,9}, Seigo Tarucha^{1,10}

¹ Center for Emergent Matter Science, RIKEN, Saitama 351-0198, Japan

² Department of Physics, Tokyo Institute of Technology, Meguro, Tokyo 152-8551, Japan

³ Advanced Device Laboratory, RIKEN, Wako, Saitama 351-0198, Japan

⁴ Department of Physics, Tokyo University of Science, Tokyo 162-8601, Japan

⁵ Department of Materials Engineering Science, Osaka University, Osaka 560-8531, Japan

⁶ Birck Nanotechnology Center, Purdue University, Indiana 47907, USA

⁷ Department of Physics and Astronomy, Purdue University, Indiana 47907, USA

⁸ School of Materials Engineering, Purdue University, Indiana 47907, USA

⁹ School of Electrical and Computer Engineering, Purdue University, Indiana 47907, USA

¹⁰ RIKEN Center for Quantum Computing, RIKEN, Saitama 351-0198, Japan

matsuo@phys.titech.ac.jp

tarucha@riken.jp

Abstract

The superconducting diode effect (SDE) is a phenomenon that has attracted significant attention for its potential to establish new Josephson junction (JJ) physics and its application as a rectifier in Josephson circuits. While many experimental platforms for SDE have been reported, only a few demonstrate high efficiency. One promising system is a JJ coherently coupled with a second JJ embedded in a superconducting loop, where SDE is controllable in direction via the phase difference. Here we study SDE in such devices under microwave irradiation. With the appearance of Shapiro steps, SDE efficiency increases as the microwave power is raised. Additionally, a finite direct current (DC) voltage difference appears without any DC bias current at high microwave powers. These results are explained by the dynamics of the JJ's washboard potential, which are common to all SDE systems. Our findings enhance the understanding of SDE dynamics and expand their potential applications.

33 A Josephson junction (JJ) is a representative superconducting (SC) device consisting of two weakly-
34 linked superconductors through insulators or normal conductors(I). JJs have been studied to engineer
35 quantum effects in solid-state devices, enabling realization of SC quantum computing and highly
36 sensitive magnetic sensors. Recently, SC diode effect (SDE) has attracted much attention as a new
37 probe of SC physics such as the Josephson effect with neither time-reversal nor spatial-inversion
38 symmetries and as a route to develop efficient rectifiers in SC circuits for applications(2–10). SDE is
39 characterized by non-reciprocal SC transport, where the critical current in the positive direction, I_{c+} ,
40 differs in the absolute value from the critical current in the negative direction, I_{c-} . Various SC devices
41 exhibit SDE based on different microscopic mechanisms, such as the vortex ratchet effect(11–14), SC
42 quantum interference(15–19), finite-momentum Cooper pairing originating from the spin-orbit
43 interactions in the presence of Zeeman splitting or ferromagnetism(6, 7, 20–28), and multiterminal
44 JJs(29–38). SDE is quantitatively characterized by the efficiency $\eta \equiv \frac{|I_{c+}| - |I_{c-}|}{|I_{c+}| + |I_{c-}|}$. Ideally, $\eta = 1$ is
45 desired for future applications but such a system is rare. Therefore, methods to significantly enhance
46 SDE efficiency η and elucidate the underlying physics are important alongside studies of the effect in
47 various candidate systems.

48 We focus on the Shapiro response(39–45) of JJs to enhance SDE efficiency η . The enhancement of
49 η in the Shapiro response has been theoretically considered in an asymmetric superconducting
50 quantum interference device (SQUID)(46, 47), which is comparable to other SDE platforms in JJs(48).
51 To discuss the critical currents of a JJ device, the resistively shunted junction (RSJ) model(49, 50) is
52 considered. The circuit is shown in Fig. 1(a). We set the JJ device in which the supercurrent $I_{sc}(\phi)$
53 has a 2π periodicity of the phase difference ϕ , contacted to a resistor R in parallel. The irradiated
54 microwave generates the alternating current (AC current) flowing in the circuit in addition to the direct
55 current (DC current) so that the bias current is written as $I_{dc} + I_{ac} \sin 2\pi ft$. I_{dc} , I_{ac} , f and t are the
56 DC current, the AC current, the frequency, and time, respectively. From the Kirchhoff's law, a sum of
57 current in the resistor and the JJ should be the bias current. From the AC Josephson effect, the voltage
58 on the JJ is described as $\frac{\hbar}{2e} \frac{d\phi}{dt}$, giving $\frac{\hbar}{2eR} \frac{d\phi}{dt} + I_{sc}(\phi) = I_{dc} + I_{ac} \sin 2\pi ft$. This equation is
59 interpreted as dynamics of a particle who moves along the ϕ axis with the washboard potential $U(\phi) -$
60 $(I_{dc} + I_{ac} \sin 2\pi ft)\phi$ with $U(\phi) = \int I_{sc}(\phi) d\phi$. This model equation means that the DC current of JJ
61 makes the washboard potential tilted, and the finite voltage appears on the JJ when the washboard
62 potential allows the particle to roll unidirectional on average. Therefore, when the JJ exhibits SDE, the
63 potential $U(\phi)$ is skewed. This model with the skewed potential produces enhancement of SDE
64 efficiency with microwave irradiation. Experimental demonstrations of the enhanced SDE by
65 microwave irradiation have been reported in a SQUID(18) and single JJs of InAs nanowires(51).

66 Here we study the Shapiro response in a system where coherently coupled JJs create SDE. The
67 coupled JJs have a device structure in which two JJs share one or two short SC electrodes(52–55). In
68 the structure, the Andreev bound states in the respective JJs are hybridized to form phase-tunable

69 Andreev molecules(56–61). Phase control of the Andreev molecules generates SDE without the need
70 for strong magnetic fields(35, 37, 62). Consequently, SDE efficiencies of around 10~30 % have been
71 experimentally obtained. We demonstrate that SDE efficiency is enhanced due to the Shapiro response.
72 The efficiency enhancement is reproduced by our numerical calculations and explained by an
73 analytical formula. These results indicate that the phase particle dynamics in the washboard potential
74 of the JJ holding SDE generate the efficiency enhancement. This will contribute to understanding of
75 SDE dynamics and development of the rectifiers useful in SC circuits.

76 The device has been fabricated from an InAs quantum well covered with an epitaxially grown
77 Aluminum film(63, 64). The device structure is depicted in Fig. 1(b). The device consists of two JJs,
78 JJ1 and JJ2. JJ2 is embedded in an SC loop to control the phase difference by an out-of-plane magnetic
79 field, B . The critical current of JJ1 which is outside of the SC loop is studied. In this device, SDE is
80 observed in JJ1 critical currents systematically as a function of B because of the Andreev molecule in
81 the two JJs(35, 37, 54, 56, 62, 65–67). We note that the critical current of JJ1 is sufficiently smaller
82 than that of the SC loop because the SC loop holds only a single JJ (JJ2) and then the critical current
83 of the SC loop should be similar to the Aluminum critical current (~ 0.1 mA) (see Appendix 8). The
84 separation between two JJs is 160 nm which is smaller than the coherence length of the Al/InAs
85 quantum well in the literature(68, 69). Then, we have measured the critical currents of JJ1 as a function
86 of B under microwave irradiation with varied power (P) and at frequency (f) (see Appendix 1 and 2).
87 The measurement has been implemented at the base temperature (~ 10 mK) in a dilution refrigerator.
88 We present results of one device in the main text and the reproducible results in a second device (see
89 Appendix 6 and 7).

90 First, we characterize the SC transport of our device. Figure 1(c) shows the voltage difference (V) on
91 JJ1 as a function of the bias direct current (I_{dc}) at $B = 0.078, 0.066, \text{ and } 0.054$ mT. The supercurrent
92 flows through JJ1 in the white region in Fig. 1(c). Clear switching behavior from the supercurrent
93 regime to the normal conduction regime is found and used to extract values for the critical current.
94 Forward and reverse critical currents I_{c+} and I_{c-} are defined as the currents at the threshold voltages
95 of $V = 1 \mu\text{V}$ and $-1 \mu\text{V}$, respectively. The evaluated absolute values of I_{c+} and I_{c-} at different B are
96 plotted in Fig. 1(d) as red and blue curves, respectively. We observe that changing B causes the critical
97 currents to oscillate due to modification of the phase difference over JJ2. The oscillation period of
98 0.144 mT is almost consistent with the period of 0.181 mT calculated from the SC loop area. The small
99 difference between the periods can be attributed to magnetic focusing from the SC leads. This is
100 because the critical current of JJ1 is modulated via Andreev molecules in JJ1 and JJ2 as already
101 reported(54). We focus on the oscillation around $B = 0$ mT to reduce the possible contribution of the
102 screening current. The bias current in the SC loop possibly produces the SDE. However, such SDE
103 contribution can be eliminated by connecting the ground to the center SC electrode, because the bias
104 current does not flow in the SC loop in this configuration (see Appendix 6 and 7).

105 SDE, $|I_{c+}| \neq |I_{c-}|$ emerges as expected from the Andreev molecules in JJ1 and JJ2. SDE efficiency
106 η can be evaluated from the results in Fig. 1(c), yielding values of $\eta = -0.15$ ($B = -0.078$ mT),

107 0.035 ($B = -0.066$ mT), and 0.14 ($B = -0.054$ mT). From the results in Fig. 1(d), η ranges from
 108 -0.15 to 0.16 for $-0.10 < B < 0.05$ mT. This result indicates that control of SDE by B can only
 109 increase $|\eta|$ to a maximum of 0.16 . We note that I_{c+} and I_{c-} do not depend on the sweep direction of
 110 I_{dc} , indicating that JJ1 is overdamped and the RSJ model is suitable for evaluating SC transport (see
 111 Appendix 3).

112 We irradiate the device with microwaves from a nearby antenna and measure the $I - V$ curves with
 113 B fixed. First, we study the $I - V$ curves at several microwave powers (P) and obtained V as a
 114 function of I_{dc} and P with microwave frequency $f = 2.5$ GHz and $B = -0.066$ mT in Figs. 1(e) and
 115 (f), respectively. At this magnetic field, SDE is almost negligible. The Shapiro steps appear at $V =$
 116 nV_0 ($n = 0, \pm 1, \pm 2$). Here $V_0 = \frac{hf}{2e} \simeq 5.17$ μ V. The $V \simeq 0$ supercurrent region can be found in the
 117 range of -5 dBm $\leq P \leq 6.5$ dBm although the transition becomes vague as P increases into the high-
 118 power regime where the Shapiro response shows oscillatory features. The image plot of Fig. 1(f) is
 119 almost symmetric to $I_{dc} = 0$ nA and therefore, $V(I_{dc} = 0)$ is always zero as confirmed in Fig. 1(e).

120 We next present the $I - V$ curves measured at several P in the range of -5 dBm $\leq P \leq 7.5$ dBm in
 121 Fig. 2(a) and the obtained V as a function of I_{dc} and P in Fig. 2(c). Here $f = 2.5$ GHz and $B =$
 122 -0.078 mT are used. Both $|I_{c+}|$ and $|I_{c-}|$ decrease and the $n = 0$ supercurrent region disappears at
 123 $P \simeq 6.5$ dBm as P increases within the range of -5 dBm $\leq P \leq 7.5$ dBm, as shown in Fig. 2(a). The
 124 Shapiro steps appear as shown in Fig. 2(c). At this magnetic field, SDE becomes pronounced. We
 125 evaluate η in the range of -5 dBm $< P < 6.5$ dBm, plotted in Fig. 2(e) with blue circles. Notably, the
 126 switching currents are well-defined within this power range while the supercurrent region becomes
 127 indistinct at the higher power regime. These results indicate that η decreases from $\eta = -0.17$ at $P =$
 128 -5 dBm with increasing P , reaching $\eta = -0.85$ at $P = 6.5$ dBm. We note that $\eta = 0$ signifies no
 129 SDE, and an increase in $|\eta|$ signifies an enhancement of SDE efficiency. Therefore, it is concluded
 130 that the microwave irradiation significantly enhances SDE efficiency. We note that the evaluated $\eta =$
 131 -0.17 at $P = -5$ dBm is slightly smaller than $\eta = -0.15$ with no irradiation. This indicates that the
 132 microwave irradiation at $P = -5$ dBm is weak but still has a discernible effect on SDE. Additionally,
 133 in Fig. 2(a), a finite positive $V = 1.7$ μ V is observed even at $I_{dc} = 0$ nA at $P = 7.5$ dBm, as indicated
 134 by the arrow. This finite positive $V(I_{dc} = 0)$ is also confirmed in Fig. 2(c) as the red region penetrating
 135 the negative current regime at $P \simeq 7.5$ dBm. This unusual behavior is not observed in the Shapiro
 136 response of JJs with the time-reversal and spatial-inversion symmetries.

137 To confirm the enhancement of SDE efficiency and $V(I_{dc} = 0) \neq 0$, we adjust B to -0.054 mT,
 138 where $|I_{c+}| > |I_{c-}|$, thus switching the polarity of SDE. We have measured the Shapiro response at
 139 the same frequency, $f = 2.5$ GHz. The measured $I - V$ curves at different P and V as a function of
 140 I_{dc} and P are shown in Figs. 2(b) and (d), respectively. The evaluated η for -5 dBm $\leq P \leq 6.5$ dBm
 141 is presented in Fig. 2(e) with red circles. In contrast to the blue circles obtained at $B = -0.078$ mT, η
 142 at $B = -0.054$ mT increases with increasing P . Importantly, the red and blue results in Fig. 2(e)
 143 exhibit the same trend: SDE efficiency is enhanced by the microwave power, as $|\eta|$ increases with P .

144 Furthermore, a finite $V(I_{dc} = 0) = -1.5 \mu\text{V}$ is also observed at $P \simeq 7.5 \text{ dBm}$ but the sign is opposite
 145 to that at $B = -0.078 \text{ mT}$. It is also confirmed that $V(I_{dc} = 0) \neq 0$ is obtained when the JJ2 phase
 146 difference is away from 0 and π (see Appendix 4). These results affirm that the observed enhancement
 147 is not an artifact in the measurement setup.

148 To validate that the observed features are intrinsic to the JJ device, we perform numerical calculations
 149 based on the RSJ model (see Appendix 5). For the calculation, we employ the current phase relation
 150 $I_{sc}(\phi, \varphi)$ of JJ1 as a function of ϕ and φ , the phase differences of JJ1 and JJ2, respectively(35, 65).
 151 We focus on the critical currents of JJ1, fixing φ and calculating the Shapiro response. The numerical
 152 results of V as a function of I_{dc} and I_{ac} at $\varphi = 0.9\pi$ and -0.9π are depicted in Figs. 3(a) and (b),
 153 respectively. The current phase relations of JJ1 at $\varphi = 0.9\pi$ and -0.9π are indicated in Fig. 3(c) with
 154 blue and red, respectively. The evaluated η from the numerical result is shown in Fig. 3(d). The
 155 calculation is in good agreement with the previously reported calculations for the asymmetric SC
 156 quantum interference device(46) and reproduces the experimentally observed features of the finite
 157 $V(I_{dc} = 0)$ and the enhancement of η . This strongly supports the notion that our experimental results
 158 are intrinsic to the JJ device.

159 To comprehend the physics of the observed features, we consider the mechanism of the Shapiro
 160 response using the washboard potential in the RSJ model ($U(\phi) - (I_{dc} + I_{ac} \sin 2\pi ft)\phi$). According
 161 to the AC Josephson effect, motion of a phase particle in the washboard potential yields a finite voltage

162 following $V = \frac{\hbar}{2e} \frac{d\phi}{dt}$. For example, the Shapiro step at $V = V_0$ in the low power regime corresponds to

163 the phase particle moving from one valley at ϕ_v of the washboard potential to the next valley at $\phi_v +$
 164 2π in a single period of $I_{ac} \sin 2\pi ft$. When the JJs exhibit no SDE, the washboard potential with $I_{dc} =$
 165 $I_{ac} = 0$ is depicted as a dashed curve in Fig.3(e). A local slope of the potential at ϕ corresponds to the
 166 supercurrent in the JJs. Then $I_{c+} = |I_{c-}|$ implies that the maximum value of the local slope equals the
 167 absolute value of the minimum local slope. We consider $U(\phi)$ of the JJs holding SDE. In this case,
 168 the maximum slope of the washboard potential differs from the minimum slope in the absolute value.
 169 This indicates that the potential is skewed due to the breaking of time-reversal and spatial-inversion
 170 symmetries. The potential of JJ1 at $\varphi = -0.9\pi$ calculated from the numerically obtained current phase
 171 relation in Fig. 3(c) is shown in Fig. 3(e) with a green curve. In this scenario, the phase particle motion
 172 is confined to the negative ϕ direction even with $I_{dc} = 0$ when $|I_{c-}| \leq I_{ac} < I_{c+}$ as depicted in Fig.
 173 3(e). Consequently, the negative $V(I_{dc} = 0)$ appears due to the AC Josephson effect. This elucidates
 174 the observed $V(I_{dc} = 0) < 0$ at $B = -0.066 \text{ mT}$ under the microwave irradiation. Therefore, the
 175 observation of finite $V(I_{dc} = 0)$ demonstrates that the JJ holds the skewed washboard potential
 176 characteristic to SDE. We note that the numerical results yield $|V(I_{dc} = 0)| = V_0$ whereas
 177 $|V(I_{dc} = 0)| \simeq 0.3 V_0$ in the experiments. This discrepancy is attributed to the thermal activation.
 178 When the thermal activation is not ignorable, the phase particle occasionally moves to the positive ϕ
 179 direction in a single cycle even with $|I_{c-}| \leq I_{ac} < I_{c+}$. This diminishes the finite $|V(I_{dc} = 0)|$ from
 180 V_0 .

181 Furthermore, the skewed $U(\phi)$ also explains the enhancement of $|\eta|$. From the above discussion
 182 using the washboard potential, I_{c+} with finite I_{ac} in $0 \leq I_{ac} \leq \max(I_{c+}, |I_{c-}|)$ is roughly determined
 183 by $I_{c+}(I_{ac} = 0) = I_{c+}(I_{ac}) + I_{ac}$ because the phase particle cannot transit over the hill to the next
 184 valley of the washboard potential until $I_{dc} + I_{ac} < I_{c+}$. Therefore, $I_{c+}(I_{ac})$ and $I_{c-}(I_{ac})$ are
 185 represented as $I_{c+}(I_{ac}) = I_{c+}(I_{ac} = 0) - I_{ac}$ and $I_{c-}(I_{ac}) = I_{c-}(I_{ac} = 0) + I_{ac}$, respectively,
 186 resulting in $\eta(I_{ac}) = \eta(I_{ac} = 0) \left(1 - \frac{2I_{ac}}{I_{c+}(I_{ac}=0) - I_{c-}(I_{ac}=0)}\right)^{-1}$. From the definition of [dBm], $I_{ac} \propto$
 187 $10^{P/20}$ is given. Then $\eta(I_{ac}) = \eta(I_{ac} = 0)(1 - a \cdot 10^{P/20})^{-1}$ is obtained(48). Here the coefficient a
 188 includes information on the critical currents with $I_{ac} = 0$ nA and the conversion efficiency of the
 189 microwave from our signal generator to I_{ac} at the JJ device, with the assumption that the conversion
 190 efficiency is constant. We implement the numerical fitting using this equation on the red and blue
 191 circles in Fig. 2(e). The blue and red dashed curves in the figures show the fitting results with
 192 $(\eta(I_{ac} = 0), a) = (-0.12, 0.42)$ and $(0.085, 0.40)$, respectively. The fitting results are in good
 193 agreement with the experimental results. This agreement indicates that the interpretation of the
 194 mechanism to produce the enhancement of η is valid. We note that the numerical fitting in Fig. 2(e)
 195 provides a smaller value of $|\eta(I_{ac} = 0)|$ than experimentally obtained. This discrepancy is attributed
 196 to the higher electron temperature during the microwave irradiation. We note that the Shapiro
 197 dynamics depending on magnetic flux in the loop in the other device has been studied and it is
 198 confirmed that the obtained $|\eta(I_{ac} = 0)|$ and a as a function of the flux show the expected dependency
 199 from the skewed washboard potential scenario (see Appendix 6).

200 Finally, we explore the Shapiro response at a higher frequency of $f = 4.0$ GHz. The $I - V$ traces
 201 with several P at $B = -0.078$ and -0.054 mT are shown in Figs. 4(a) and (b), respectively.
 202 Additionally, image plots of V as a function of I_{dc} and P at $B = -0.078$ and -0.054 mT are
 203 displayed in Figs. 4(c) and (d), respectively. Furthermore, the evaluated η at $B = -0.078$ and -0.054
 204 mT as a function of P is shown with blue and red circles in Fig. 4(e). The enhancement of SDE is still
 205 observed as shown in Fig. 4(e). On the other hand, $V(I_{dc} = 0) = 1.0$ and -0.52 μ V at $B = -0.078$
 206 and -0.054 mT at $f = 4.0$ GHz in Figs. 4(a) and (b) are less distinguishable than $V(I_{dc} = 0) = 1.7$
 207 and -1.5 μ V obtained at $f = 2.5$ GHz in Figs. 2(a) and (b), respectively. The fitting results with
 208 $(\eta(I_{ac} = 0), a) = (-0.13, 1.41)$ and $(0.077, 1.39)$ for the blue and red circles are indicated as blue
 209 and red curves in Fig. 4(e). The observed $\eta(I_{ac} = 0)$ is not much different from the results at $f = 2.5$
 210 GHz. Therefore, the less distinguishable $V(I_{dc} = 0)$ is not attributed to elevated electron temperature
 211 at the higher f . Instead it may be assigned to the phase particle motion originating from the capacitance
 212 parallel to the JJ. When the frequency becomes higher, the time-periodic change of the washboard
 213 potential becomes faster. When the parallel capacitance, C , is included in the RSJ model, the additional
 214 term of $\frac{\hbar C}{2e} \frac{d^2 \phi}{dt^2}$ acts as an acceleration of the phase particle. Then the phase particle cannot follow the
 215 change of the potential landscape and then cannot move out of the bottom of the valley even with

216 $I_{c+} \leq I_{ac} < -I_{c-}$.

217 In summary, we experimentally explore the Shapiro response of SDE using coupled JJ devices
218 fabricated from an InAs quantum well covered with an epitaxially grown Aluminum film. We find two
219 major features: enhancement of η and finite $V(I_{dc} = 0)$ in the response, which cannot be found in the
220 Shapiro response of JJs with no SDE. Our numerical calculation based on the RSJ model with the
221 current phase relation of the coupled JJ reproduces the two major features. The anomalous response
222 can be attributed to the phase particle dynamics in the skewed washboard potential of the JJs with SDE.
223 The demonstrated method and underlying physics are applicable to SDE in various JJ devices. It is
224 noted that this method decreases the critical current while the SDE efficiency increases. Therefore, it
225 would not be a great solution to realize rectifiers useful in SC circuits but our results contribute to
226 establishing the fundamental physics of dynamics in SDE systems.

227

228 **Appendix**

229 **1. Sample growth, device fabrication, and measurement setup**

230 The wafer has been grown on a semi-insulating InP substrate by molecular beam epitaxy. The stack
231 materials from the bottom to top are a 100 nm $\text{In}_{0.52}\text{Al}_{0.48}\text{As}$ buffer, a 5 period 2.5 nm $\text{In}_{0.53}\text{Ga}_{0.47}\text{As}/2.5$
232 nm $\text{In}_{0.52}\text{Al}_{0.48}\text{As}$ superlattice, a 1 μm thick metamorphic graded buffer stepped from $\text{In}_{0.52}\text{Al}_{0.48}\text{As}$ to
233 $\text{In}_{0.84}\text{Al}_{0.16}\text{As}$, a 33 nm graded $\text{In}_{0.84}\text{Al}_{0.16}\text{As}$ to $\text{In}_{0.81}\text{Al}_{0.19}\text{As}$ layer, a 25 nm $\text{In}_{0.81}\text{Al}_{0.19}\text{As}$ layer, a 4 nm
234 $\text{In}_{0.81}\text{Ga}_{0.19}\text{As}$ lower barrier, a 5 nm InAs quantum well, a 10 nm $\text{In}_{0.81}\text{Ga}_{0.19}\text{As}$ top barrier, two
235 monolayers of GaAs and finally an 8.7 nm layer of epitaxial Al. The top Al layer has been grown in
236 the same chamber without breaking the vacuum. A two-dimensional electron gas (2DEG) is
237 accumulated in the InAs quantum well layer.

238 In the fabrication process, we have performed wet etching of the unnecessary epitaxial Aluminum
239 with a type-D aluminum etchant to form JJs and SC loops with conventional electron beam lithography
240 techniques.

241 For the microwave irradiation, we have installed a high-frequency coaxial line in our dilution fridge.
242 The coaxial line is made of NbTi (coax Co., Ltd). Two attenuators (XMA) have been inserted in the
243 line. 20 dB, and 5 dB attenuators have been attached on the 4K plate, and 100 mK plate in our fridge,
244 respectively. We have injected the rf power from our signal generator (Anapico APSIN20G). We note
245 that 10 mK of our base temperature does not mean 10 mK of the electron temperature.

246

247 **2. Device structure**

248 An optical image of our device is indicated in Fig. 5(a). The SC loop consists of JJ2 and the SC leads
249 with 600 nm width. The loop is described with the dashed rectangular in Fig. 5(a). The SC loop area S is
250 $11.4 \mu\text{m}^2$. The expected period of the critical current oscillation is calculated as $2\pi BS/\Phi_0 = 0.18 \text{ mT}$.
251 Our observed period is slightly smaller than the expected value likely due to the effect of flux focusing or
252 the wider loop area than the design due to the side etching in the Aluminum wet etching process. JJ1 and
253 JJ2 are both fabricated with 1.6 μm width and 80 nm junction length. The shared SC lead has a 160 nm

254 separation between JJ1 and JJ2. The distance is much shorter than the bulk coherence length of Aluminum
 255 ($\sim 1 \mu\text{m}$).

256 257 3. The $I - V$ curves obtained with the different I_{dc} sweep directions

258 The $I - V$ curves can hold hysteresis to the current sweep direction when there is a parallel capacitance
 259 in addition to the RSJ model (namely, when we consider the resistively and capacitively shunted model).
 260 In this case, I_{c+} (I_{c-}) should be defined from the $I - V$ curve with the positive (negative) sweep direction.
 261 Then it is necessary to confirm if the hysteresis is observed in our measurement setup or not.

262 Figure 5(b) represents the $I - V$ curves obtained with $f = 2.5 \text{ GHz}$ in $-5 \leq P \leq -20 \text{ dBm}$ at $B =$
 263 -0.054 mT . The circles and lines with the same colors are obtained with the positive and negative current
 264 sweeps at the same P , respectively. The circles and lines obtained at the same P are highlighted with the
 265 same colors. Then hysteresis can appear when the circles and lines with the same colors are compared. In
 266 the results, the difference between circles and lines is less compared to the data resolution. Namely, the
 267 hysteresis is ignorable, meaning that JJ1 is highly overdamped and it is justified to use the RSJ model instead
 268 of the RCSJ model for the numerical calculation to reproduce our experimental results.

269 270 4. $V(I_{dc} = 0)$ as a function of P and B

271 To verify that the finite $V(I_{dc} = 0)$ depends on the current phase relation modulated from the JJ2 phase
 272 difference, we measured the $V(I_{dc} = 0)$ as a function of P in $-0.09 < B < 0.09 \text{ mT}$ at $f = 2.5 \text{ GHz}$.
 273 Figure 5(c) indicates the obtained $V(I_{dc} = 0)$. $V(I_{dc} = 0)$ becomes significant above the noise of V in the
 274 range of $5 < P < 10 \text{ dBm}$. Importantly, the sign of $V(I_{dc} = 0)$ becomes opposite around $B =$
 275 -0.066 mT and 0 mT . These points correspond to the time-reversal symmetric conditions that SDE has
 276 not been observed at 0 or π of the JJ2 phase difference. This result means that the finite $V(I_{dc} = 0)$ is one
 277 of the features in the dynamics observed in SDE device. This supports our conclusion that the observed
 278 Shapiro response discussed in the main text is derived from the JJ1 current phase relation modulated by
 279 JJ2 through Andreev molecules.

280 281 5. Numerical calculation of the current phase relation

282 We performed the numerical calculation based on the RSJ model as discussed in the main text. The
 283 calculation is based on the normalized RSJ model with $\tau \equiv 2eRI_c t / \hbar$ as

$$284 \quad \frac{d\phi}{d\tau} + \frac{I_{sc}(\phi)}{I_c} = \frac{I_{dc}}{I_c} + \frac{I_{ac}}{I_c} \sin 2\pi f \frac{\hbar}{2eRI_c} \tau$$

285 Here I_c is the critical current. $I_{sc}(\phi)$ is calculated from the two-dimensional current phase relation,
 286 $I_{sc}(\phi, \varphi)$ of the coupled JJs calculated from the tight-binding model studied in our previous
 287 reports(35, 65). For the calculation in Figs. 3(a) and (b), the current phase relations of the JJs in the RSJ
 288 model are given as $I_{sc}(\phi, \varphi = 0.9\pi)$ and $I_{sc}(\phi, \varphi = -0.9\pi)$, which are shown in Fig.3(c). We
 289 performed the calculations with $RI_c = 30 \mu\text{V}$ and $f = 2.5 \text{ GHz}$.

290

291 6. Reproducibility in a different device

292 We checked the data reproducibility with a different device B. To confirm the reproducibility, we
293 fabricated the device with a slightly different structure from the device discussed in the main text. The
294 structure of the device B is depicted in Fig. 6(a). JJ1 and JJ2 are fabricated with $1.2\ \mu\text{m}$ width and $70\ \text{nm}$
295 junction length. The shared SC lead has a $160\ \text{nm}$ separation between JJ1 and JJ2.

296 We put two gate electrodes on JJ1 and JJ2 for local control of the JJs and other gate electrodes ($G_{2\text{deg}}$) to
297 deplete electrons in the InAs quantum well other than the JJs. For the below experiments, we always apply
298 $-4\ \text{V}$ on the gate $G_{2\text{deg}}$. For the measurement, we used a different dilution refrigerator and electronics.
299 Especially, we used a small local superconducting solenoid coil to induce the magnetic flux in the SC loop
300 to control the phase difference of JJ2 (we used an SC magnet in the main text).

301 Figure 6(c) indicates SDE observed in device B. In this device and setup, hysteresis is observed in the
302 $I - V$ traces due to the underdamped behavior. Then we define the positive and negative switching
303 currents, $I_{\text{sw}+}$ and $I_{\text{sw}-}$, from the traces obtained with the current sweep from negative to positive and vice
304 versa, respectively. The positive and negative retrap currents, I_{r+} and I_{r-} , are also evaluated from the
305 traces with the negative and positive sweep of the bias current, respectively. SDE which is dependent on
306 the phase difference of JJ2 controlled by the voltage on the solenoid coil, V_{coil} is observed as expected
307 from the coherent coupling between two JJs.

308 The Shapiro responses of SDE at $V_{\text{coil}} = -1.27$ and $-0.46\ \text{V}$ are studied. The microwave of $f = 3\ \text{GHz}$ is
309 irradiated for the Shapiro response measurements. The observed V as a function of I and P at $V_{\text{coil}} = -1.27$
310 V ($-0.46\ \text{V}$) with the different current sweep directions are exhibited in Figs. 7(a) and (c) ((b) and (d)).
311 From the results, the evaluated SC diode efficiency η as a function of P at both V_{coil} values is shown in
312 Fig. 8(a) with the solid curves. $\eta(I_{\text{ac}} = 0)$ and a obtained by the numerical fitting are represented in Fig.
313 8(b). We note that no error bar for $a=0$ on $V_{\text{coil}} = -0.94\ \text{V}$ indicates that the bar exceeds the plot
314 bounds. At this condition, η vs. P does not change rapidly and so a is ineffective in the fitting. As
315 expected, the obtained $\eta(I_{\text{ac}} = 0)$ as a function of V_{coil} follows the trend of the SDE with no microwave
316 irradiation in Fig. 6(c). The obtained a in Fig. 8(b) increases as V_{coil} changes to reduce $|I_{\text{sw}}|$ except for
317 $V_{\text{coil}} \approx -1\ \text{V}$ where the SDE vanishes. This derives from $a \propto (|I_{\text{sw}+}(I_{\text{ac}} = 0)| + |I_{\text{sw}-}(I_{\text{ac}} = 0)|)^{-1}$.
318 Due to this relation, the smaller $|I_{\text{sw}}|$ produces larger a . Then, this dependency also supports that the
319 phase particle dynamics in the skewed washboard generates the peculiar Shapiro dynamics including the
320 SDE efficiency enhancement.

321

322 7. Difference between device A and device B

323 Since our device includes the SC loop, one can imagine that the bias current in the SC loop in device A can
324 produce the SDE and the observed SDE is not related to the AMS. To confirm that our SDE originates from
325 the AMS, we consider the structures of device A and device B. We observed the SDE also in device B
326 whose structure differs slightly from that of device A. In device A, discussed in the main manuscript,
327 the bias current induced from the upper SC electrode in Fig.1(b) flows through JJ1 to the GND
328 connected to the lower part of the SC loop. In this case, the trivial contribution from the SC loop

329 inductance including the phase shift of JJ2 by the bias current should be considered, as you pointed
330 out. On the other hand, in device B (Fig. 6(a)), the bias current is induced from the upper SC electrode,
331 with the GND connected to the center electrode. We described the device structures in Fig. 6(b). In
332 this configuration, the bias current does not flow through JJ2 and the SC loop. Additionally, we have
333 studied another device in which the position of JJ2 is shifted to make 1 μm of a distance between JJ1
334 and JJ2 in Fig. S13 of our previous paper(35). If the bias current in the SC loop were responsible for
335 the SDE, we could expect the finite SDE in the data. However, in the device, no SDE is observed.
336 Then the bias current in the SC loop is eliminated as the source of the observed SDE. Only the coherent
337 coupling of JJ1 and JJ2 can affect JJ2 because the bias current in JJ1 changes ϕ , modifying the
338 supercurrent and φ in JJ2 through the AMS. In device B, we observed the SDE and the same features
339 in the Shapiro response. Then we conclude that we demonstrated the Shapiro response of the SDE
340 from the AMS.

341

342 **8. Critical current in the shared SC lead**

343 We measured the $I - V$ trace of the JJ device consisting of the 1 μm -width SC lead on the same Al/InAs
344 quantum well with the larger bias current range as shown in Fig. 9. A small jump occurs at $I_{\text{dc}} = 0.6 \text{ mA}$
345 corresponding to the critical current in our SC leads of the loop. Since the width of this loop is 1 μm , the
346 critical current of the shared SC lead whose width is 160 nm can be estimated as around 0.1 mA. This is
347 sufficiently large compared with the bias current used in our experiment discussed in the main text
348 ($\sim 0.6 \mu\text{A}$). Then we ignore the screening current effect in the shared SC lead because the screening current
349 should be smaller than the critical current of JJ2 which is comparable with that in JJ1.

350

351 **Acknowledgments**

352 Funding: This work was partially supported by a JSPS Grant-in-Aid for Scientific Research (S)
353 (Grant No. JP19H05610); JST FOREST; the Murata Science Foundation; the US Department of
354 Energy under Award No. DE-SC0019274.

355

356 **Competing interest statement**

357

358 The authors declare no competing interests.

359

360 **References**

- 361 1. B. D. Josephson, Possible new effects in superconductive tunnelling. *Phys. Lett.* **1**, 251–253
362 (1962).
- 363 2. R. Wakatsuki, Y. Saito, S. Hoshino, Y. M. Itahashi, T. Ideue, M. Ezawa, Y. Iwasa, N. Nagaosa,
364 Nonreciprocal charge transport in noncentrosymmetric superconductors. *Science Advances* **3**,
365 e1602390 (2017).
- 366 3. F. Ando, Y. Miyasaka, T. Li, J. Ishizuka, T. Arakawa, Y. Shiota, T. Moriyama, Y. Yanase, T.
367 Ono, Observation of superconducting diode effect. *Nature* **584**, 373–376 (2020).
- 368 4. T. Golod, V. M. Krasnov, Demonstration of a superconducting diode-with-memory, operational
369 at zero magnetic field with switchable nonreciprocity. *Nat Commun* **13**, 3658 (2022).
- 370 5. J.-X. Lin, P. Siriviboon, H. D. Scammell, S. Liu, D. Rhodes, K. Watanabe, T. Taniguchi, J. Hone,
371 M. S. Scheurer, J. I. A. Li, Zero-field superconducting diode effect in small-twist-angle trilayer
372 graphene. *Nat. Phys.* **18**, 1221–1227 (2022).
- 373 6. B. Pal, A. Chakraborty, P. K. Sivakumar, M. Davydova, A. K. Gopi, A. K. Pandeya, J. A. Krieger,
374 Y. Zhang, M. Date, S. Ju, N. Yuan, N. B. M. Schröter, L. Fu, S. S. P. Parkin, Josephson diode
375 effect from Cooper pair momentum in a topological semimetal. *Nat. Phys.* **18**, 1228–1233 (2022).
- 376 7. B. Turini, S. Salimian, M. Carrega, A. Iorio, E. Strambini, F. Giazotto, V. Zannier, L. Sorba, S.
377 Heun, Josephson Diode Effect in High Mobility InSb Nanoflags. *Nano Lett.* **22**, 8502–8508
378 (2022).
- 379 8. A. Daido, Y. Ikeda, Y. Yanase, Intrinsic Superconducting Diode Effect. *Phys. Rev. Lett.* **128**,
380 037001 (2022).
- 381 9. H. Narita, J. Ishizuka, R. Kawarazaki, D. Kan, Y. Shiota, T. Moriyama, Y. Shimakawa, A. V.
382 Ognev, A. S. Samardak, Y. Yanase, T. Ono, Field-free superconducting diode effect in
383 noncentrosymmetric superconductor/ferromagnet multilayers. *Nat. Nanotechnol.* **17**, 823–828
384 (2022).
- 385 10. M. Davydova, S. Prembabu, L. Fu, Universal Josephson diode effect. *Sci. Adv.* **8**, eabo0309
386 (2022).
- 387 11. G. Carapella, G. Costabile, Ratchet Effect: Demonstration of a Relativistic Fluxon Diode.
388 *Physical Review Letters* **87**, 077002 (2001).
- 389 12. M. Beck, E. Goldobin, M. Neuhaus, M. Siegel, R. Kleiner, D. Koelle, High-Efficiency
390 Deterministic Josephson Vortex Ratchet. *Physical Review Letters* **95**, 090603 (2005).

- 391 13. A. Sterck, D. Koelle, R. Kleiner, Rectification in a Stochastically Driven Three-Junction SQUID
392 Rocking Ratchet. *Physical Review Letters* **103**, 047001 (2009).
- 393 14. A. Sterck, R. Kleiner, D. Koelle, Three-Junction SQUID Rocking Ratchet. *Physical Review*
394 *Letters* **95**, 177006 (2005).
- 395 15. M. D. Thompson, M. B. Shalom, A. K. Geim, A. J. Matthews, J. White, Z. Melhem, Y. A. Pashkin,
396 R. P. Haley, J. R. Prance, Graphene-based tunable SQUIDs. *Applied Physics Letters* **110**, 162602
397 (2017).
- 398 16. A. Murphy, A. Bezryadin, Asymmetric nanowire SQUID: Linear current-phase relation,
399 stochastic switching, and symmetries. *Physical Review B* **96**, 094507 (2017).
- 400 17. C. Ciaccia, R. Haller, A. C. C. Drachmann, T. Lindemann, M. J. Manfra, C. Schrade, C.
401 Schönenberger, Gate Tunable Josephson Diode in Proximitized InAs Supercurrent
402 Interferometers. *Phys. Rev. Research* **5**, 033131 (2023).
- 403 18. M. Valentini, O. Sagi, L. Baghumyan, T. De Gijssel, J. Jung, S. Calcaterra, A. Ballabio, J. Aguilera
404 Servin, K. Aggarwal, M. Janik, T. Adletzberger, R. Seoane Souto, M. Leijnse, J. Danon, C.
405 Schrade, E. Bakkers, D. Chrastina, G. Isella, G. Katsaros, Parity-conserving Cooper-pair
406 transport and ideal superconducting diode in planar germanium. *Nat Commun* **15**, 169 (2024).
- 407 19. F. Paolucci, G. De Simoni, F. Giazotto, A gate- and flux-controlled supercurrent diode effect.
408 *Applied Physics Letters* **122**, 042601 (2023).
- 409 20. C. Baumgartner, L. Fuchs, A. Costa, S. Reinhardt, S. Gronin, G. C. Gardner, T. Lindemann, M.
410 J. Manfra, P. E. F. Junior, D. Kochan, J. Fabian, N. Paradiso, C. Strunk, Supercurrent rectification
411 and magnetochiral effects in symmetric Josephson junctions. *Nature Nanotechnology*, doi:
412 10.1038/s41565-021-01009-9 (2021).
- 413 21. H. Wu, Y. Wang, Y. Xu, P. K. Sivakumar, C. Pasco, U. Filippozzi, S. S. P. Parkin, Y.-J. Zeng,
414 T. McQueen, M. N. Ali, The field-free Josephson diode in a van der Waals heterostructure.
415 *Nature* **604**, 653–656 (2022).
- 416 22. A. Costa, C. Baumgartner, S. Reinhardt, J. Berger, S. Gronin, G. C. Gardner, T. Lindemann, M.
417 J. Manfra, J. Fabian, D. Kochan, N. Paradiso, C. Strunk, Sign reversal of the Josephson
418 inductance magnetochiral anisotropy and $0-\pi$ -like transitions in supercurrent diodes. *Nat.*
419 *Nanotechnol.* **18**, 1266–1272 (2023).
- 420 23. A. Buzdin, Direct Coupling Between Magnetism and Superconducting Current in the
421 Josephson Junction. *Physical Review Letters* **101**, 107005 (2008).

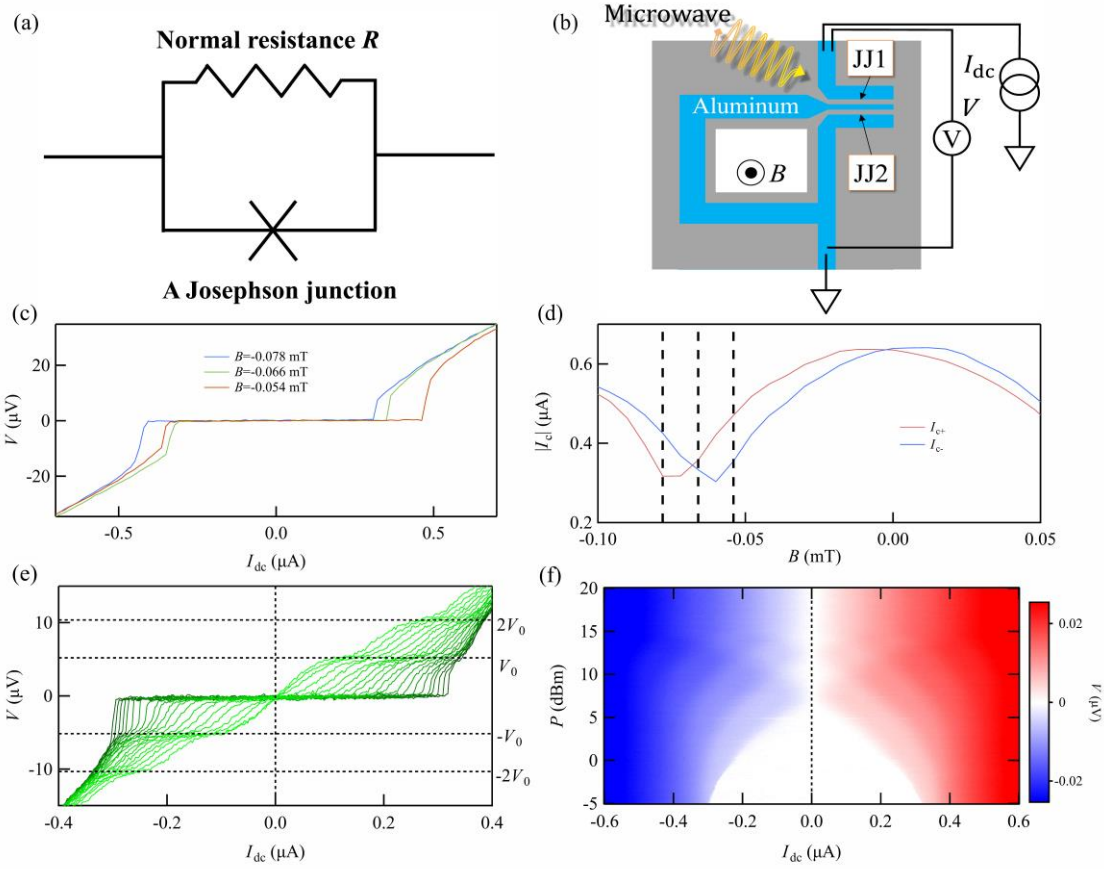
- 422 24. A. Zazunov, R. Egger, T. Jonckheere, T. Martin, Anomalous Josephson Current through a Spin-
423 Orbit Coupled Quantum Dot. *Phys. Rev. Lett.* **103**, 147004 (2009).
- 424 25. Y. Tanaka, T. Yokoyama, N. Nagaosa, Manipulation of the Majorana Fermion, Andreev
425 Reflection, and Josephson Current on Topological Insulators. *Physical Review Letters* **103**,
426 107002 (2009).
- 427 26. T. Yokoyama, M. Eto, Y. V. Nazarov, Anomalous Josephson effect induced by spin-orbit
428 interaction and Zeeman effect in semiconductor nanowires. *Physical Review B* **89**, 195407 (2014).
- 429 27. J. J. He, Y. Tanaka, N. Nagaosa, A phenomenological theory of superconductor diodes. *New J.*
430 *Phys.* **24**, 053014 (2022).
- 431 28. H. F. Legg, D. Loss, J. Klinovaja, Superconducting diode effect due to magnetochiral anisotropy
432 in topological insulators and Rashba nanowires. *Phys. Rev. B* **106**, 104501 (2022).
- 433 29. A. W. Draelos, M.-T. Wei, A. Seredinski, H. Li, Y. Mehta, K. Watanabe, T. Taniguchi, I. V.
434 Borzenets, F. Amet, G. Finkelstein, Supercurrent Flow in Multiterminal Graphene Josephson
435 Junctions. *Nano Letters* **19**, 1039–1043 (2019).
- 436 30. N. Pankratova, H. Lee, R. Kuzmin, K. Wickramasinghe, W. Mayer, J. Yuan, M. G. Vavilov, J.
437 Shabani, V. E. Manucharyan, Multiterminal Josephson Effect. *Physical Review X* **10** (2020).
- 438 31. G. V. Graziano, J. S. Lee, M. Pendharkar, C. J. Palmstrøm, V. S. Pribiag, Transport studies in a
439 gate-tunable three-terminal Josephson junction. *Physical Review B* **101** (2020).
- 440 32. J. Chiles, E. G. Arnault, C.-C. Chen, T. F. Q. Larson, L. Zhao, K. Watanabe, T. Taniguchi, F.
441 Amet, G. Finkelstein, Non-Reciprocal Supercurrents in a Field-Free Graphene Josephson Triode.
442 *Nano Lett.*, acs.nanolett.3c01276 (2023).
- 443 33. F. Zhang, A. S. Rashid, M. T. Ahari, W. Zhang, K. M. Ananthanarayanan, R. Xiao, G. J. de
444 Coster, M. J. Gilbert, N. Samarth, M. Kayyalha, Andreev processes in mesoscopic multi-terminal
445 graphene Josephson junctions. *Phys. Rev. B* **107**, L140503 (2023).
- 446 34. M. Gupta, G. V. Graziano, M. Pendharkar, J. T. Dong, C. P. Dempsey, C. Palmstrøm, V. S.
447 Pribiag, Gate-tunable superconducting diode effect in a three-terminal Josephson device. *Nat*
448 *Commun* **14**, 3078 (2023).
- 449 35. S. Matsuo, T. Imoto, T. Yokoyama, Y. Sato, T. Lindemann, S. Gronin, G. C. Gardner, M. J.
450 Manfra, S. Tarucha, Josephson diode effect derived from short-range coherent coupling. *Nat.*
451 *Phys.*, doi: 10.1038/s41567-023-02144-x (2023).

- 452 36. M. Kocsis, Z. Scherübl, G. Fülöp, P. Makk, S. Csonka, Strong nonlocal tuning of the current-
453 phase relation of a quantum dot based Andreev molecule. arXiv arXiv:2303.14842 [Preprint]
454 (2023). <http://arxiv.org/abs/2303.14842>.
- 455 37. M. Coraiola, A. E. Svetogorov, D. Z. Haxell, D. Sabonis, M. Hinderling, S. C. Ten Kate, E. Cheah,
456 F. Krizek, R. Schott, W. Wegscheider, J. C. Cuevas, W. Belzig, F. Nichele, Flux-Tunable
457 Josephson Diode Effect in a Hybrid Four-Terminal Josephson Junction. *ACS Nano* **18**, 9221–
458 9231 (2024).
- 459 38. A. S. Rashid, L. Yi, T. Taniguchi, K. Watanabe, N. Samarth, R. Mélin, M. Kayyalha, Exploring
460 nonequilibrium Andreev resonances in ultraclean graphene Andreev interferometers. arXiv
461 arXiv:2405.02975 [Preprint] (2024). <http://arxiv.org/abs/2405.02975>.
- 462 39. S. Shapiro, Josephson Currents in Superconducting Tunneling: The Effect of Microwaves and
463 Other Observations. *Phys. Rev. Lett.* **11**, 80–82 (1963).
- 464 40. M. J. Renne, D. Polder, Some analytical results for the resistively shunted Josephson junction.
465 *Rev. Phys. Appl. (Paris)* **9**, 25–28 (1974).
- 466 41. J. R. Waldram, P. H. Wu, An alternative analysis of the nonlinear equations of the current-driven
467 Josephson junction. *J Low Temp Phys* **47**, 363–374 (1982).
- 468 42. E. Bocquillon, R. S. Deacon, J. Wiedenmann, P. Leubner, T. M. Klapwijk, C. Brune, K. Ishibashi,
469 H. Buhmann, L. W. Molenkamp, Gapless Andreev bound states in the quantum spin Hall
470 insulator HgTe. *Nature Nanotechnology* **12**, 137–143 (2016).
- 471 43. K. Ueda, S. Matsuo, H. Kamata, Y. Sato, Y. Takeshige, K. Li, L. Samuelson, H. Xu, S. Tarucha,
472 Evidence of half-integer Shapiro steps originated from nonsinusoidal current phase relation in a
473 short ballistic InAs nanowire Josephson junction. *Phys. Rev. Research* **2**, 033435 (2020).
- 474 44. M. C. Dartailh, J. J. Cuzzo, B. H. Elfeky, W. Mayer, J. Yuan, K. S. Wickramasinghe, E. Rossi,
475 J. Shabani, Missing Shapiro steps in topologically trivial Josephson junction on InAs quantum
476 well. *Nat Commun* **12**, 78 (2021).
- 477 45. Y. Takeshige, S. Matsuo, R. S. Deacon, K. Ueda, Y. Sato, Y.-F. Zhao, L. Zhou, C.-Z. Chang, K.
478 Ishibashi, S. Tarucha, Experimental study of ac Josephson effect in gate-tunable (Bi_{1-x}Sb_x)
479 ₂Te₃ thin-film Josephson junctions. *Phys. Rev. B* **101**, 115410 (2020).
- 480 46. R. S. Souto, M. Leijnse, C. Schrade, Josephson Diode Effect in Supercurrent Interferometers.
481 *Phys. Rev. Lett.* **129**, 267702 (2022).
- 482 47. J. J. Cuzzo, W. Pan, J. Shabani, E. Rossi, Microwave-tunable diode effect in asymmetric

- 483 SQUIDs with topological Josephson junctions. *Phys. Rev. Research* **6**, 023011 (2024).
- 484 48. R. Seoane Souto, M. Leijnse, C. Schrade, M. Valentini, G. Katsaros, J. Danon, Tuning the
485 Josephson diode response with an ac current. *Phys. Rev. Research* **6**, L022002 (2024).
- 486 49. W. C. Stewart, CURRENT-VOLTAGE CHARACTERISTICS OF JOSEPHSON JUNCTIONS.
487 *Appl. Phys. Lett.* **12**, 277–280 (1968).
- 488 50. D. E. McCumber, Effect of ac Impedance on dc Voltage-Current Characteristics of
489 Superconductor Weak-Link Junctions. *Journal of Applied Physics* **39**, 3113–3118 (1968).
- 490 51. H. Su, J.-Y. Wang, H. Gao, Y. Luo, S. Yan, X. Wu, G. Li, J. Shen, L. Lu, D. Pan, J. Zhao, P.
491 Zhang, H. Q. Xu, Microwave-assisted unidirectional superconductivity in Al-InAs nanowire-Al
492 junctions under magnetic fields. arXiv arXiv:2402.02137 [Preprint] (2024).
493 <http://arxiv.org/abs/2402.02137>.
- 494 52. K. Ueda, S. Matsuo, H. Kamata, S. Baba, Y. Sato, Y. Takeshige, K. Li, S. Jeppesen, L. Samuelson,
495 H. Xu, S. Tarucha, Dominant nonlocal superconducting proximity effect due to electron-electron
496 interaction in a ballistic double nanowire. *Science Advances* **5**, eaaw2194 (2019).
- 497 53. O. Kürtössy, Z. Scherübl, G. Fülöp, I. E. Lukács, T. Kanne, J. Nygård, P. Makk, S. Csonka,
498 Andreev Molecule in Parallel InAs Nanowires. *Nano Lett.* **21**, 7929–7937 (2021).
- 499 54. S. Matsuo, J. S. Lee, C.-Y. Chang, Y. Sato, K. Ueda, C. J. Palmstrøm, S. Tarucha, Observation
500 of nonlocal Josephson effect on double InAs nanowires. *Commun Phys* **5**, 221 (2022).
- 501 55. R. Debbarma, A. Tsintzis, M. Aspegren, R. S. Souto, S. Lehmann, K. Dick, M. Leijnse, C.
502 Thelander, Josephson Junction $\pi - 0$ Transition Induced by Orbital Hybridization in a Double
503 Quantum Dot. *Phys. Rev. Lett.* **131**, 256001 (2023).
- 504 56. J.-D. Pillet, V. Benzoni, J. Griesmar, J.-L. Smirr, Ç. O. Girit, Nonlocal Josephson Effect in
505 Andreev Molecules. *Nano Letters* **19**, 7138–7143 (2019).
- 506 57. V. Kornich, H. S. Barakov, Y. V. Nazarov, Overlapping Andreev states in semiconducting
507 nanowires: Competition of one-dimensional and three-dimensional propagation. *Physical Review*
508 *B* **101**, 195430 (2020).
- 509 58. V. Kornich, H. S. Barakov, Y. V. Nazarov, Fine energy splitting of overlapping Andreev bound
510 states in multiterminal superconducting nanostructures. *Physical Review Research* **1**, 033004
511 (2019).
- 512 59. S. Matsuo, T. Imoto, T. Yokoyama, Y. Sato, T. Lindemann, S. Gronin, G. C. Gardner, S. Nakosai,

- 513 Y. Tanaka, M. J. Manfra, S. Tarucha, Phase-dependent Andreev molecules and superconducting
514 gap closing in coherently-coupled Josephson junctions. *Nat Commun* **14**, 8271 (2023).
- 515 60. M. Coraiola, D. Z. Haxell, D. Sabonis, H. Weisbrich, A. E. Svetogorov, M. Hinderling, S. C. Ten
516 Kate, E. Cheah, F. Krizek, R. Schott, W. Wegscheider, J. C. Cuevas, W. Belzig, F. Nichele,
517 Phase-engineering the Andreev band structure of a three-terminal Josephson junction. *Nat*
518 *Commun* **14**, 6784 (2023).
- 519 61. M. Coraiola, D. Z. Haxell, D. Sabonis, M. Hinderling, S. C. ten Kate, E. Cheah, F. Krizek, R.
520 Schott, W. Wegscheider, F. Nichele, Spin-degeneracy breaking and parity transitions in three-
521 terminal Josephson junctions. arXiv arXiv:2307.06715 [Preprint] (2023).
522 <http://arxiv.org/abs/2307.06715>.
- 523 62. J.-D. Pillet, S. Annabi, A. Peugeot, H. Riechert, E. Arrighi, J. Griesmar, L. Bretheau, Josephson
524 diode effect in Andreev molecules. *Phys. Rev. Research* **5**, 033199 (2023).
- 525 63. M. Kjaergaard, F. Nichele, H. J. Suominen, M. P. Nowak, M. Wimmer, A. R. Akhmerov, J. A.
526 Folk, K. Flensberg, J. Shabani, C. J. Palmstrom, C. M. Marcus, Quantized conductance doubling
527 and hard gap in a two-dimensional semiconductor?superconductor heterostructure. *Nature*
528 *Communications* **7**, 12841 (2016).
- 529 64. M. Kjaergaard, H. J. Suominen, M. P. Nowak, A. R. Akhmerov, J. Shabani, C. J. Palmstrøm, F.
530 Nichele, C. M. Marcus, Transparent Semiconductor-Superconductor Interface and Induced Gap
531 in an Epitaxial Heterostructure Josephson Junction. *Phys. Rev. Applied* **7**, 034029 (2017).
- 532 65. S. Matsuo, T. Imoto, T. Yokoyama, Y. Sato, T. Lindemann, S. Gronin, G. C. Gardner, M. J.
533 Manfra, S. Tarucha, Phase engineering of anomalous Josephson effect derived from Andreev
534 molecules. *Sci. Adv.* **9**, eadj3698 (2023).
- 535 66. D. Z. Haxell, M. Coraiola, M. Hinderling, S. C. Ten Kate, D. Sabonis, A. E. Svetogorov, W.
536 Belzig, E. Cheah, F. Krizek, R. Schott, W. Wegscheider, F. Nichele, Demonstration of the
537 Nonlocal Josephson Effect in Andreev Molecules. *Nano Lett.* **23**, 7532–7538 (2023).
- 538 67. E. W. Hodt, J. Linder, On-off switch and sign change for a nonlocal Josephson diode in spin-
539 valve Andreev molecules. *Phys. Rev. B* **108**, 174502 (2023).
- 540 68. W. Mayer, J. Yuan, K. S. Wickramasinghe, T. Nguyen, M. C. Dartiailh, J. Shabani,
541 Superconducting proximity effect in epitaxial Al-InAs heterostructures. *Applied Physics Letters*
542 **114**, 103104 (2019).
- 543 69. W. Mayer, M. C. Dartiailh, J. Yuan, K. S. Wickramasinghe, E. Rossi, J. Shabani, Gate controlled

544 anomalous phase shift in Al/InAs Josephson junctions. *Nature Communications* **11**, 212 (2020).
545
546
547

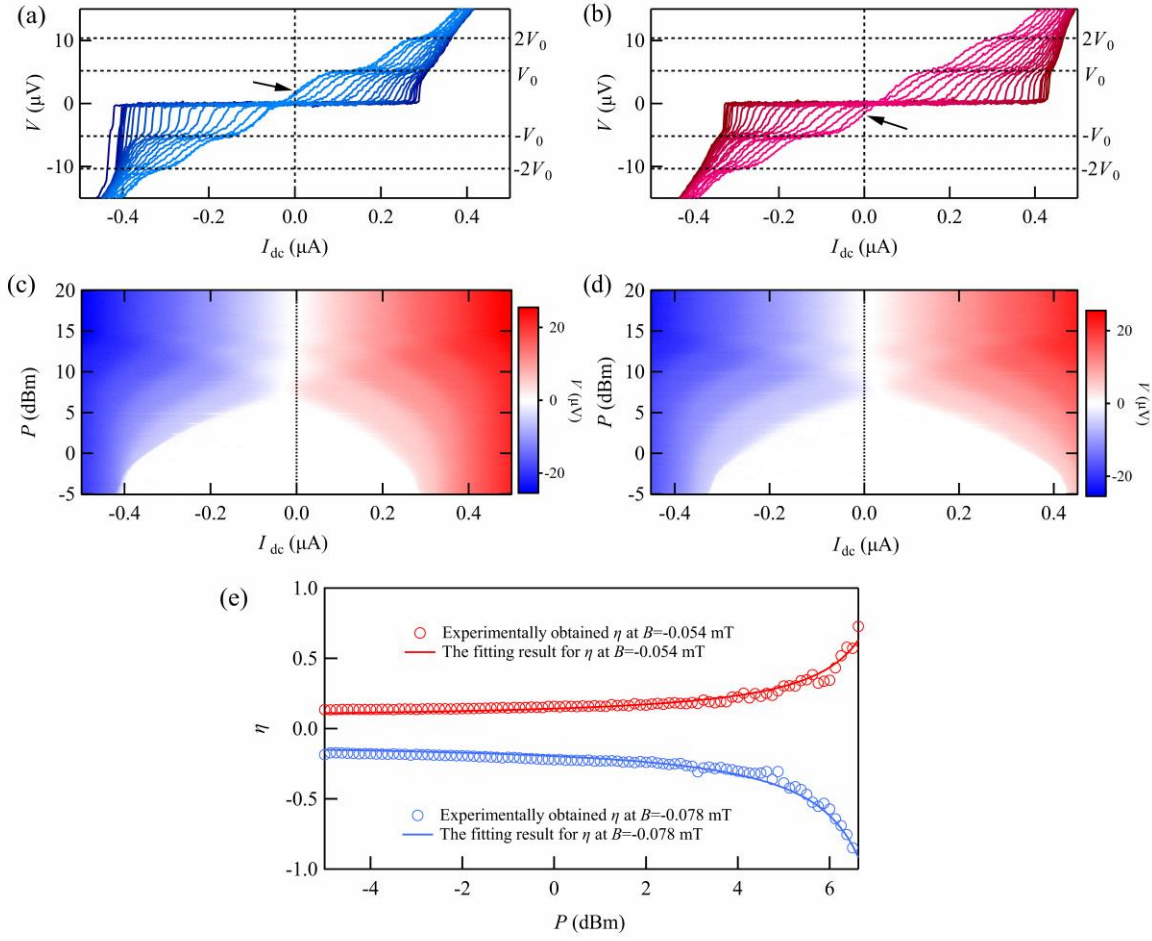


549

550

551 **Fig. 1.** (a) is an electrical circuit for the resistively shunted junction model. (b) is a schematic image
 552 of our device structure and measurement setup. The blue and grey regions indicate the quantum well
 553 wafer surfaces with and without Aluminum thin film. (c) shows $I - V$ traces at $B =$
 554 $-0.078, -0.066,$ and -0.054 mT with no irradiation with blue, green, and red curves, respectively.
 555 (d) represents I_{c+} and I_{c-} in the absolute value as a function of B with red and blue curves,
 556 respectively. (e) indicates $I - V$ traces at $B = -0.066$ mT with the microwave irradiation of $f =$
 557 2.5 GHz at several P in $-5 \text{ dBm} \leq P \leq 7.5 \text{ dBm}$. (f) is V as a function of I_{dc} and P . The image plot is
 558 almost symmetric to $I_{dc} = 0$ nA.

559



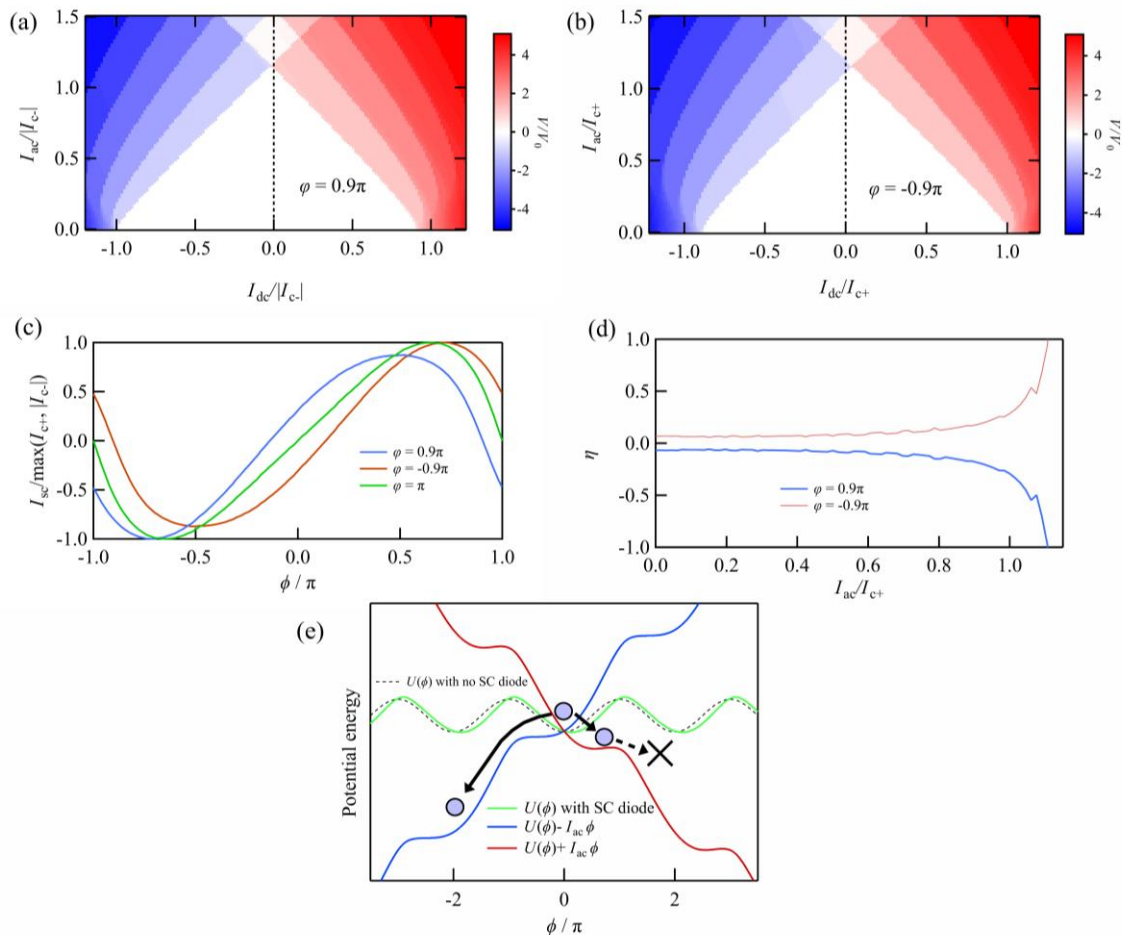
560

561 **Fig. 2.** (a) and (b) indicate $I - V$ traces at $f = 2.5$ GHz in $-5 \text{ dBm} \leq P \leq 7.5 \text{ dBm}$ at $B = -0.078$
 562 and -0.054 mT, respectively. The darker blue curves are obtained at smaller P . $V(I_{dc} = 0)$ becomes
 563 finite at $P = 7.5$ dBm as arrowed. (c) and (d) show image plots of V as a function of I_{dc} and P at
 564 $B = -0.078$ and -0.054 mT, respectively. The images are asymmetric to $I_{dc} = 0$ nA. The red region
 565 in (c) and the blue region in (d) penetrates the negative and positive I_{dc} regime in the vicinity of $P =$
 566 7.5 dBm, respectively. (e) shows evaluated η as a function of P at $B = -0.078$ and -0.054 mT with
 567 blue and red circles, respectively. The solid curves indicate the fitting results.

568

569

570



571

572

573 **Fig. 3.** The numerical results of V as a function of I_{dc} and P with $\varphi = 0.9\pi$ and -0.9π are shown in

574 (a) and (b), respectively. (c) represents the current phase relation of JJ1 as a function of ϕ at $\varphi =$

575 $\pm 0.9\pi$, which is used for (a) and (b). The green curve indicates the current phase relation at $\varphi = \pi$.

576 (d) indicates η evaluated from the results. (e) exhibits the potential landscape of $U(\phi)$ for the JJ

577 without and with SDE, $U(\phi) - I_{ac}\phi$ with SDE, and $U(\phi) + I_{ac}\phi$ with SDE represented by the

578 dashed black, solid green, red, and blue curves, respectively. $U(\phi)$ with SDE is calculated from the

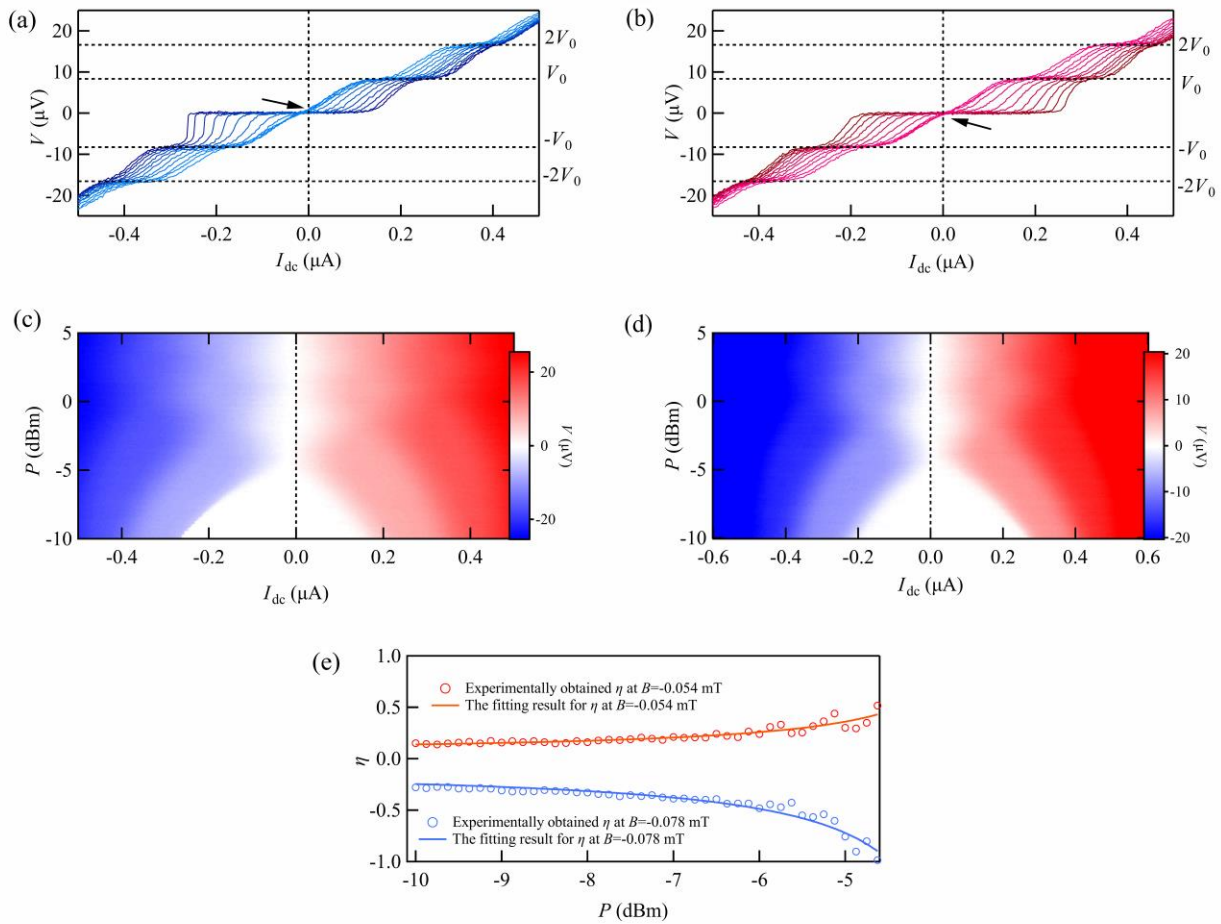
579 current phase relation of JJ1 at $\varphi = -0.9\pi$. The image corresponds to the situation of $|I_{c-}| < I_{ac} <$

580 I_{c+} . The phase particle rolls the blue landscape to the negative ϕ direction while it does not go out of

581 the valley in the red case.

582

583



584

585

586 **Fig. 4.** (a) and (b) show $I - V$ traces at $f = 4.0$ GHz in -10 dBm $\leq P \leq -3.0$ dBm at $B = -0.078$
 587 and -0.054 mT, respectively. (c) and (d) represent image plots of V as a function of I_{dc} and P at $B =$
 588 -0.078 and -0.054 mT, respectively. (e) is evaluated η as a function of P at $B = -0.078$ and
 589 -0.054 mT with blue and red circles, respectively. The solid curves indicate the fitting results.

590

591
 592
 593
 594
 595
 596
 597
 598
 599
 600
 601
 602
 603
 604
 605
 606
 607
 608
 609
 610
 611
 612
 613
 614
 615
 616
 617
 618
 619

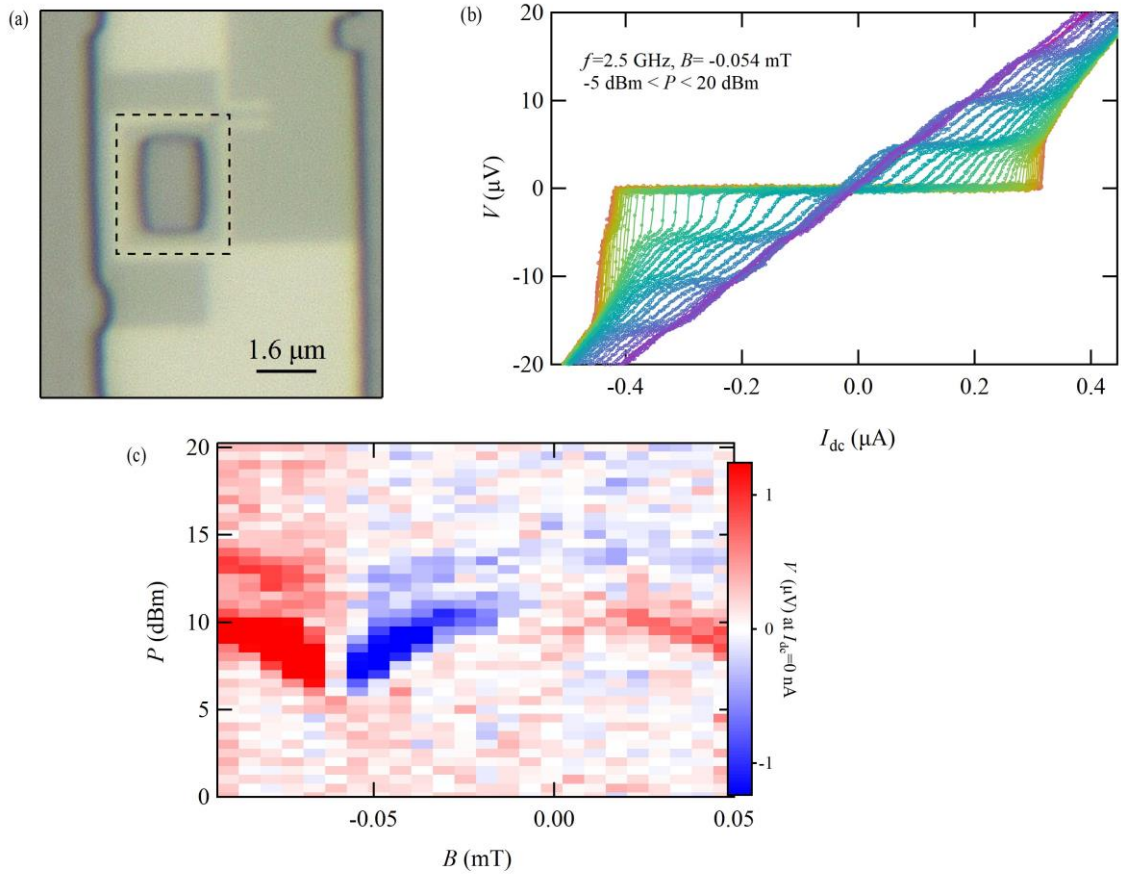
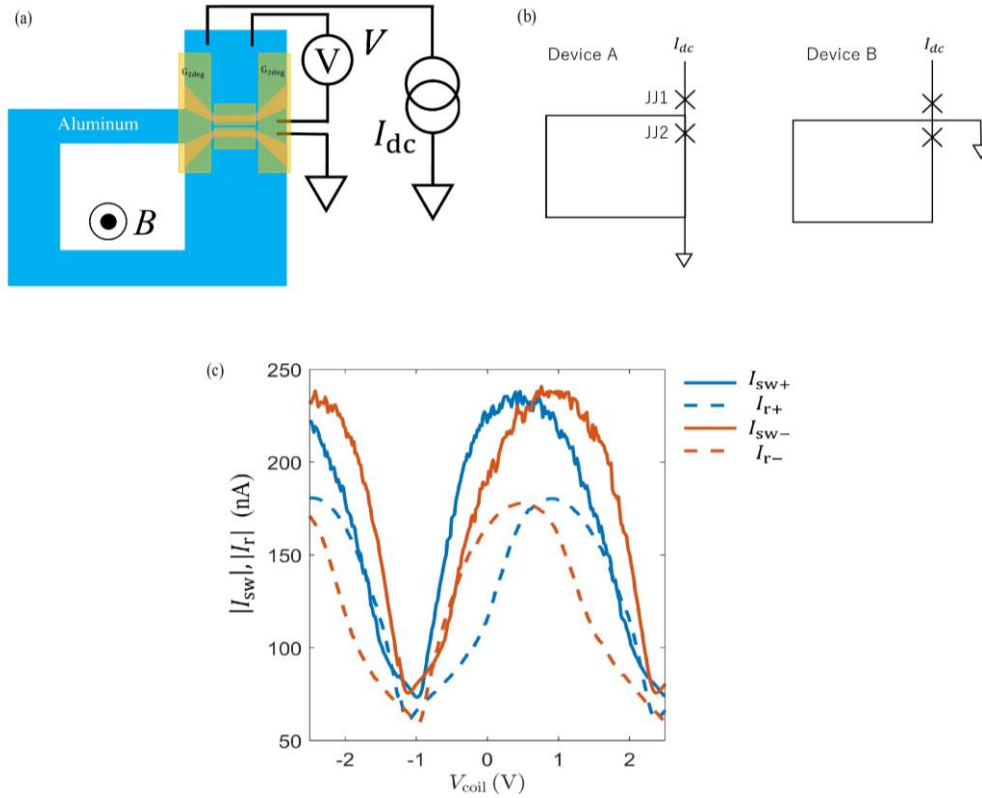


Fig. 5: (a) An optical image of the device. The white and gray regions are the Aluminum electrodes and the naked InAs well, respectively. The dark gray regions were deeply etched to form the mesa. (b) The obtained V as a function of I_{dc} in $-5 < P < 20$ dBm. The circles and lines with the same colors represent the results obtained with the positive and negative current sweep, respectively. There is little difference between the circles and lines, meaning ignorable hysteresis in the $I - V$ traces. (c) V at $I_{dc} = 0$ as a function of P and B at $f = 2.5$ GHz. The finite voltage appears when the phase difference of JJ2 is away from $\varphi = 0, \pi$.



620 Fig. 6: (a) A schematic image of device B. We depleted the carriers in the two dimensional electron gas other than
 621 the Josephson junctions by using a gate (G_{2deg}). (b) Schematic diagrams of device A and device B. In the configuration
 622 of device A, the bias current flows in the SC loop while the current does not flow in the loop in the device B case.
 623 (c) Observed I_{sw+} and I_{sw-} as a function of the magnetic flux in the SC loop controlled by V_{coil} . The retrap currents,
 624 I_{r+} and I_{r-} are also exhibited.

625
 626
 627
 628
 629
 630
 631
 632
 633
 634
 635
 636
 637
 638
 639
 640

641
642
643
644
645
646
647
648
649
650
651
652
653
654
655
656
657
658
659
660
661
662
663
664
665

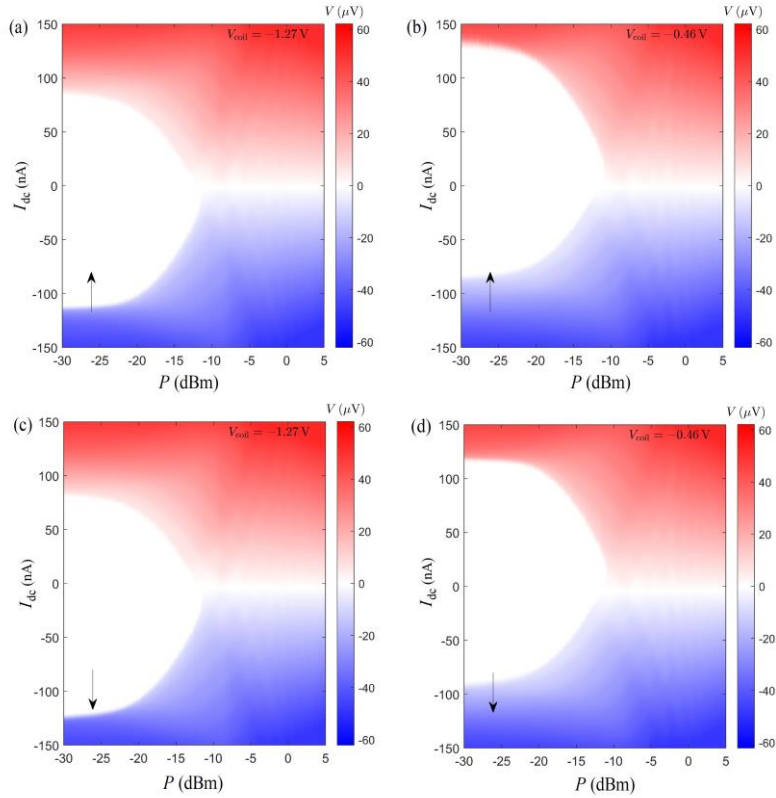
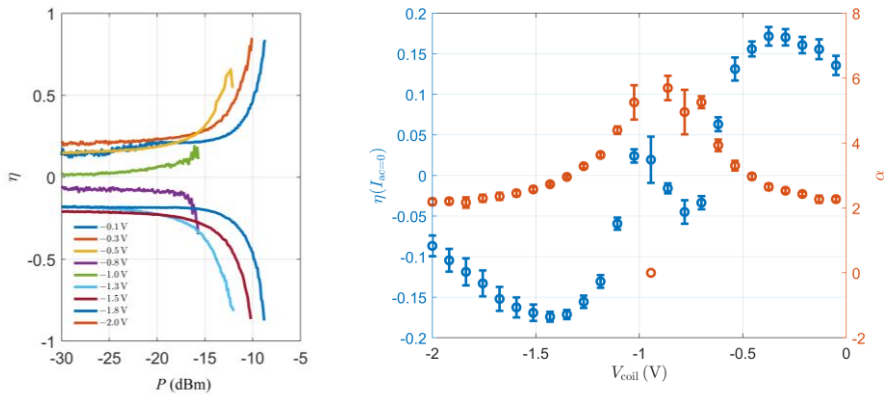


Fig. 7: (a) and (c) represent V as a function of P and I_{dc} at $V_{coil} = -1.27$ V with $f = 3$ GHz with the current sweep direction along the black arrows. (b) and (d) represent V as a function of P and I_{dc} at $V_{coil} = -0.46$ V with $f = 3$ GHz with the current sweep direction along the black arrows.



666 Fig. 8: (a) The curves are the evaluated η from the experimental data at $V_{coil} = -0.1, -0.3, -0.5, -0.8, -1.0,$
667 $-1.3, -1.5, -1.8, -2.0$ V as a function of P . (b) $\eta(I_{ac} = 0)$ and α obtained by the numerical fitting on the
668 curve of η as a function of P .
669
670

671
672
673
674
675
676
677
678
679
680
681
682

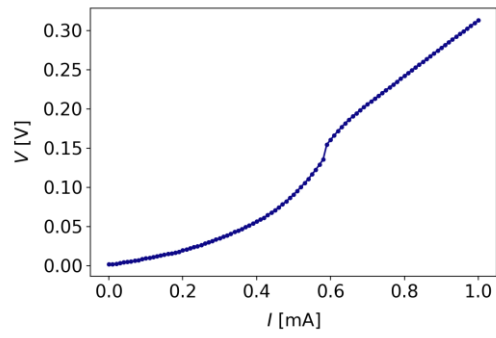


Fig. 9: The obtained $I - V$ trace of the JJ device with 1 μm -width SC lead.